AIAA SciTech Forum
7-11 January 2019, San Diego, California
AIAA Scitech 2019 Forum

10.2514/6.2019-2081

Effects of blade load distributions on wind turbine wake evolution using a blade resolved CFD simulations

Anthony P. Edmonds*, Arash Hassanzadeh, Andrew C. Kirby,
Dimitri J. Mavriplis, Jonathan Naughton
Department of Mechanical Engineering, University of Wyoming, Laramie, WY 82071, USA

An analysis of a pair of small-scale turbines designed using blade element momentum theory is performed using blade-resolved numerical simulation. Analysis on the wake structures are studied using Reynolds stress analysis to compare the differences due to differing blade load distribution. The results show that relatively small differences in blade loading can lead to significant differences in wake structures which persist far downstream. This implies that extreme care should be taken to match experimental blade loading with industrial scale turbine loading.

I. Introduction

Wind turbine wake interaction is important to the service lifetime of wind turbines; the turbulence intensity of the incoming flow can reduce service life, increased noise emission due to blade-vortex interactions, and result in a reduction of harvested energy from the loss of kinetic energy of the incoming flow. To understand wake behavior, experimental studies need to be carried out. However, full-scale experiments are costly and are limited to only providing global information about the flow. Computational Fluid Dynamics (CFD) simulations can be performed to gather detailed information upstream and downstream of the turbine. CFD also allows for modeling the variability in atmospheric conditions, wind farm layout, and wake studies.

The wake structure of a turbine is assumed to depend primarily on the thrust coefficient C_T. The spanwise loading distribution may also affect the wake behavior. Wake sensitivity to blade load distributions was studied by Kelly et al.[1] A free-wake vortex lattice method was applied to two turbines, one with higher load near the blade tip, to simulate the wake behind them. The result showed differences in the wake structures. A large-eddy simulation was performed on the turbines designed in Ref[1] by Yang et al. [2] The resulting wakes showed considerable differences in the axial velocity, rotational velocity, and turbulent kinetic energy for the two designs. Neither of the above models can capture the blade loading, which was treated as an input to the models to simulate the wake. Blade resolved CFD simulations are capable of capturing the correct blade loading, and therefore are important to wind turbine wake studies.

The goal of this work is to use a blade resolved CFD simulation to study the effect of different load distributions on the wake of wind turbines. Two small scale turbines were designed to have nearly the same thrust coefficients, but to have different blade load distributions. The turbines were then simulated using identical flow conditions, and solver settings, including mesh refinement criteria, refinement levels, and solution order.

II. Numerical Methodology

The **W**yoming **W**ind and **A**erospace **A**pplications **K**omputation **E**nvironment (W^2A^2KE3D)[3] was used in this work. This software framework allows for high-fidelity blade-resolved wind turbine simulations[4] and W^2A^2KE3D 's suitability and performance has been demonstrated in previous work with a 48 turbine wind farm with full blade resolution on 22,000 cores,[3] and has scaled up to 144 wind turbines on 67,000 cores. In addition the framework has been applied to aerospace applications.[5,6]

*Corresponding author: aedmond4@uwyo.edu

The framework uses an overset grid paradigm, supporting the use of an unstructured *near-body* CFD solver, and a Cartesian *off-body* solver, shown in Figure 1. This allows for the complex geometry and the boundary layer of the turbine blades to be captured with adequate resolution. This is coupled with an off-body-solver that is computationally efficient, and capable of dynamic mesh refinement. The use of multiple meshes enables effective use of mesh and solver application in a wide range of conditions, particularly in wind energy applications.

The near-body solver, NSU3D,[7,8] is an unstructured finite-volume solver for the Unsteady Reynolds Averaged Navier-Stokes equations. NSU3D is capable of running several turbulence models: Spalart-Allmaras (SA),[9] K-Omega,[10] and the Delayed Detached Eddy Simulation (DDES)[11] turbulence models with rotation/curvature correction.[12]

The off-body solver is referred to as DG4est,[5] which is a high-order discontinuous Galerkin finite-element method solver for the compressible Navier-Stokes Equations. It is capable of mesh (h) refinement via the *p4est*[13,14] adaptive mesh refinement framework, along with its own order (p) adaption, and thus has *hp*-adaption capabilities. DG4est uses a Constant Smagorinsky Large Eddy Simulation[15] turbulence model. These two CFD solvers are linked by TIOGA,[16–18] an overset mesh assembler, which dynamically interpolates the solutions between the meshes.

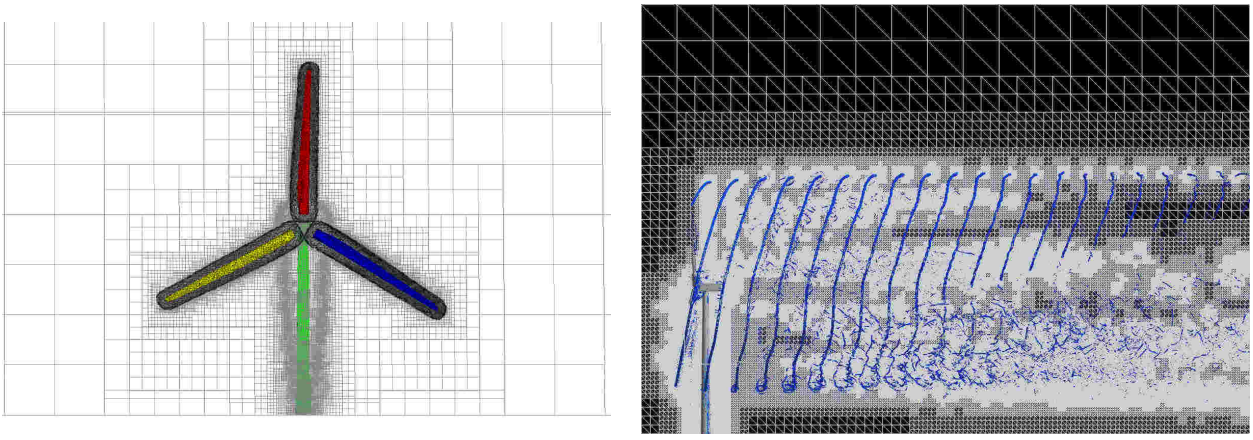

Figure 1. Overset mesh technology used to incorporate complex geometry and dynamic mesh adaption for wake capturing.

III. Problem Description

Two different blade designs were meshed with a nose cone, with all three blades centered in one unstructured mesh for each turbine design. Care was taken to minimize differences between the meshes, with Design A being composed of 6,559,094 tetrahedra,118,910 pyramids, and 20,826,268 prisms making up just under 12 million nodes. Design B is composed of just under 7 million nodes with 3,026,614 tetrahedra, 179,139 pyramids, and 12,593,194 prisms. The mesh around design B is shown in Figure 2. The meshes are trimmed to extend 0.3 m from the blade, given a blade length of 1 m, where the mesh intersects with the background Cartesian mesh.

Identical initial conditions, boundary conditions, and solver settings were used for both simulations. In both cases, the wind turbine tower and nacelle were omitted for simplicity. The incoming flow was uniform and laminar, the fluid was taken as an ideal air with a density of 1.225 kg/m^3, and a kinematic viscosity of $1.47 \cdot 10^{-5} m^2/s$. The turbines were oriented with the inflow heading perpendicular to the rotor's plane of revolution. The turbines are relatively small scale with a rotor diameter of 2 m, and rotate at 804 rpm. A global time step was used that corresponds to 1/3° rotor rotation. At each time step the solution is interpolated between the near-body and off-body meshes by the overset mesh assembler. The off-body solver uses a fourth-order accurate Runge-Kutta four-stage explicit timestepping scheme and a Constant Smagorinsky Large Eddy Simulation[15] turbulence model. The discontinuous Galerkin flow solver supports p-refinement, which is used to smoothly transition away from the near-body mesh. Second-order ($p = 1$) accurate polynomials are used near the blade surface, transitioning by use of $p = 2$ order polynomials, ending at $p = 3$, fourth-order polynomials in mesh cells away from the surface. The near-body solver utilizes

(a) (b)

Figure 2. Small-scale wind turbine Design B unstructured blade mesh with 7 million nodes. a) Overall mesh structure b) Blade tip mesh

the second-order accurate Backwards Difference Formula method to implicitly timestep to the global step. It uses a Delayed Detached Eddy Simulation[11] turbulence model. Previous work has shown this spatial and temporal resolution is the minimum necessary resolution to obtain accurate turbine power and thrust predictions.[3]

IV. Results

IV.A. Blade Design

The turbine blades were designed using an inverse blade element momentum theory. The blades have different blade load distributions, as shown in Figure 3. However they have nearly the same integrated force value (thrust coefficient). Design A has higher normal forces in the tip region than Design B (See Figure 3) (a). The distribution of tangential force can be seen in Figure 3 (b). The forces in these figures were obtained using a blade element (BEM) design approach.[19] BEM theory combines the local consideration of a chord-wise blade profile (blade element) and conservation of momentum.[19] It is commonly used to design and analyze wind turbine blades and propellers. Design B is achieved by modifying Design A's geometry, which is described in detail in Hassanzadeh et al.[19] The instantaneous forces from the CFD simulation, shown in Figure 4 show a similar magnitude and profile to the expected forces from the design.

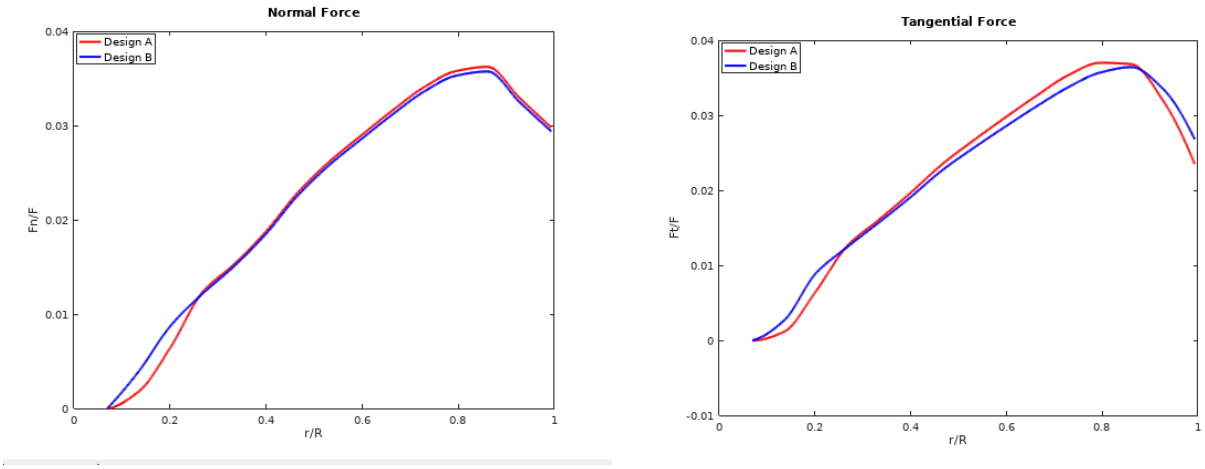

(a) (b)

Figure 3. Forces from BEM theory (a) Normalized normal and (b) tangential force distributions for Design A and Design B.

IV.B. Wake Analysis

The near-body mesh for Design A was partitioned into 1,188 cores. Initially, the off-body solver was run with 11,160 cores containing over 11 million degrees of freedom. As the off body mesh grew through AMR to just under 1 billion degrees of freedom the solver was run on 16,740 cores. This simulation was run for thirty-two 12-hour runs, corresponding to 57,724 time steps or just over 53 rotor revolutions.

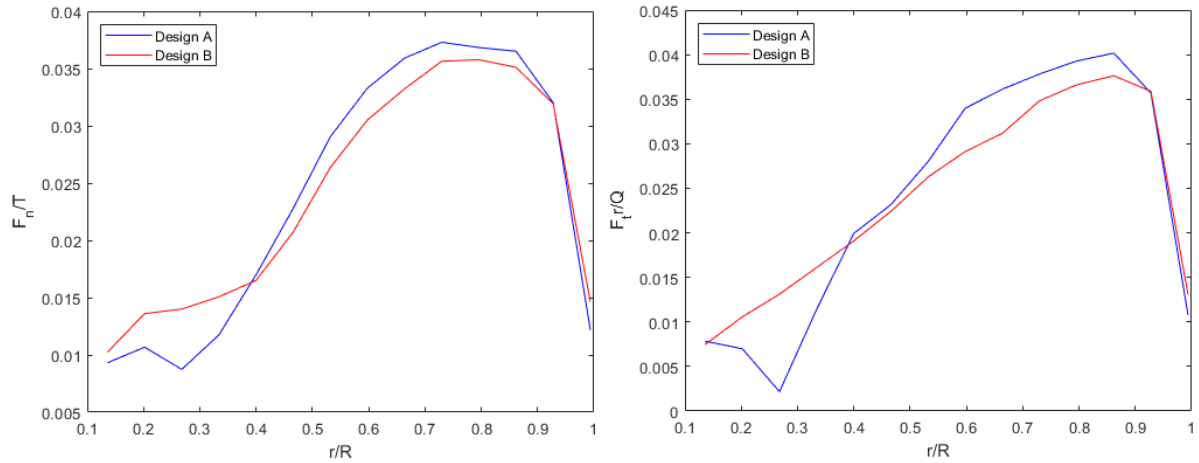

(a)

Figure 4. Resulting forces calculated from CFD Simulation (a) Normalized normal and (b) tangential force distributions for Design A and Design B.

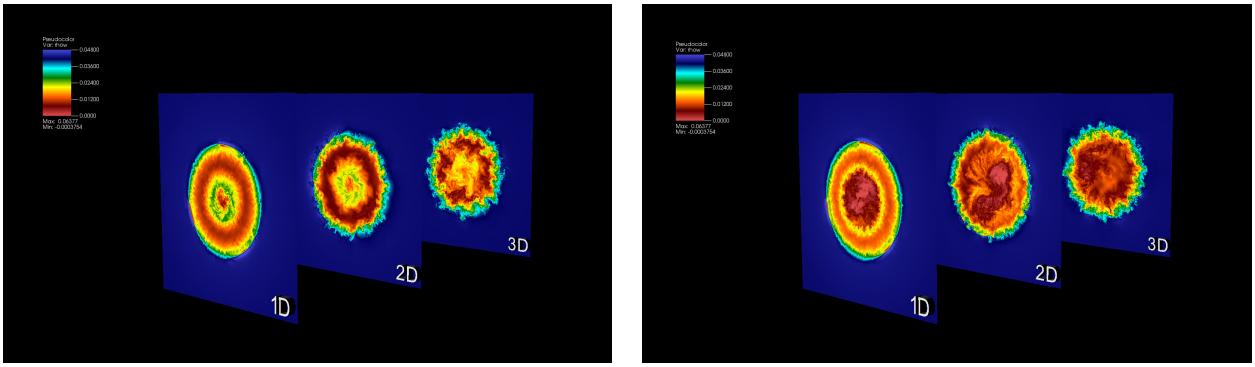

(a) Design A (b) Design B

Figure 5. Instantaneous axial momentum distribution at multiple downstream positions, annotated by rotor diameter lengths (D).

Design B's near-body mesh was partitioned on 720 cores. As with Design A, the off-body solver was initially run with 11,160 cores for just under 11 million degrees of freedom, and the core count increased to 16,740 cores with 1 billion degrees of freedom. The simulation for Design B was run for thirty-two 12-hour runs yielding just over 53 revolutions in 57,601 time steps.

Slices of the wake were collected at downstream locations. Figure 5 shows the instantaneous axial momentum at the first three downstream diameters (D) for the two designs. The wake structure is coherent in the near wake region to one rotor diameter (1D) downstream for both designs. For design A, the normal force is higher in the tip region, which can be seen in Figure 5, with design A having a lower axial velocity, and therefore has a higher capture of flow energy. Near the root region, the axial velocity is higher in Design A than in Design B, which can be seen in both Figures 5 and 6. Design B has higher forces in the root region, and as shown in Figure 3, this causes the wake structure to break down faster near the root region of the flow. Moving downstream, vortex merging and hopping occur, showing the instability of the vortex structures.

The differences in the wake are analyzed by collecting slices over two rotor revolutions at every 2° rotor

revolution. This generates 720 samples per set, and data was collected for three sets generating a total of 2,160 temporal slices per station. The instantaneous absolute tangential velocity is shown in Figure 6, where the flow direction is from left to right. In the near wake, tip vorticies are clearly defined, and break down as they travel downstream. Figure 7 is an isocontour of velocity magnitude of 12 m/s colored by density. This shows the tip vorticies remain strongly defined until about half way between stations 1D and 2D, after this point they have broken down. This is consistent with the observations in the wake slices, i.e. the vortex structures are unstable and merging and hopping occur.

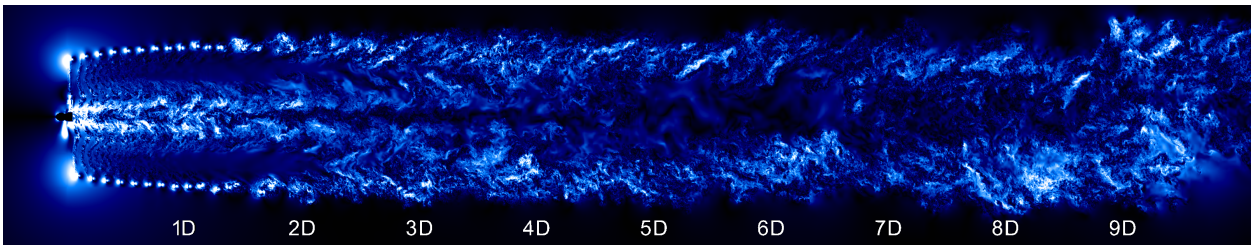

(a) Design A

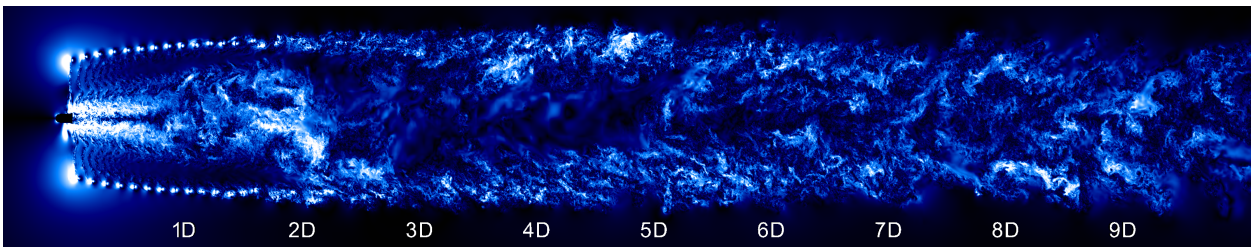

(b) Design B

Figure 6. Instantaneous absolute tangential velocity demonstrating the wake propagation downstream, annotated by rotor diameter lengths (D).

Figure 8 shows a slice-by-slice comparison of the instantaneous axial velocity of the two designs. In the near wake at half a rotor diameter downstream, the center axial velocity of Design B is higher than for Design A. Moving along the radius of the blade, the axial velocity becomes lower for Design B until about half the blade span. From the half span to the tip, the axial velocity is lower for Design A. Moving further downstream to one rotor diameter the core of the wake for Design B has disappeared completely. However, for Design A that core remains strongly defined, but the mid radius wake deficit has increased. At two rotor diameters downstream, Design A still has the core wake structure, while at the same point in the wake of Design B there is no coherent structure.

A similar behavior is shown in Figure 9, which shows the instantaneous radial velocity. The tangential velocity behavior is also important to the wake behavior. Figure 9 shows that for both designs, the tip region is dominated by the effect of the tip vorticies for 0.5D and 1D. By 2D, that structure has completely broken down in both cases, which is in agreement with Figure 6. However, the structure in the tip area in Design A appears to take up a larger radial extent than in Design B. This appears to be in close agreement with the loading shown in Figure 4, where the tip loading is higher in Design A. As with the axial velocity in the core, the core region of the tangential velocity for Design B has undergone a complete change at 2D.

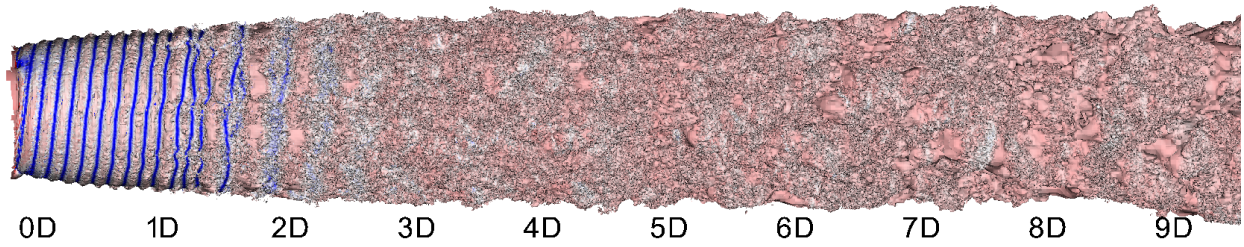

(a) Design A

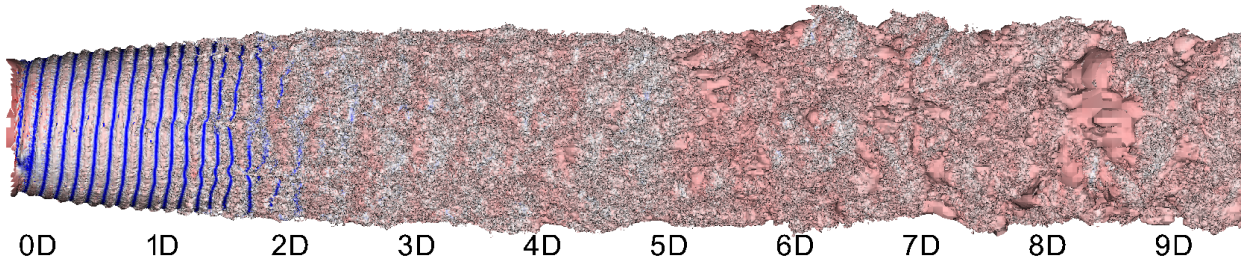

(b) Design B

Figure 7. Instantaneous isocontour of the velocity magnitude 12 m/s using density to color. Blue is lower density, and red is higher density.

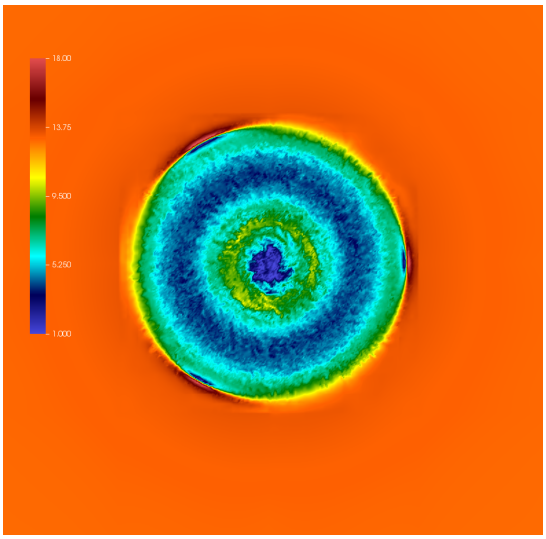

(a) 0.5D - Design A

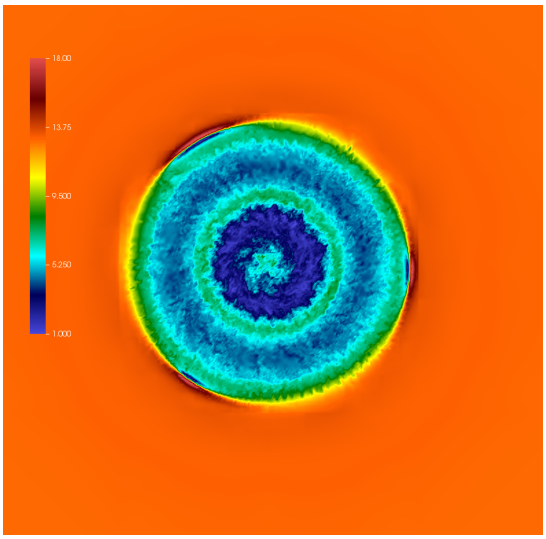

(b) 0.5D - Design B

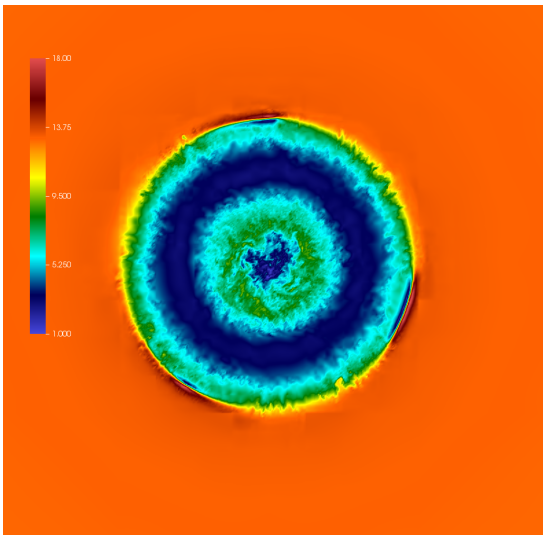

(c) 1D - Design A

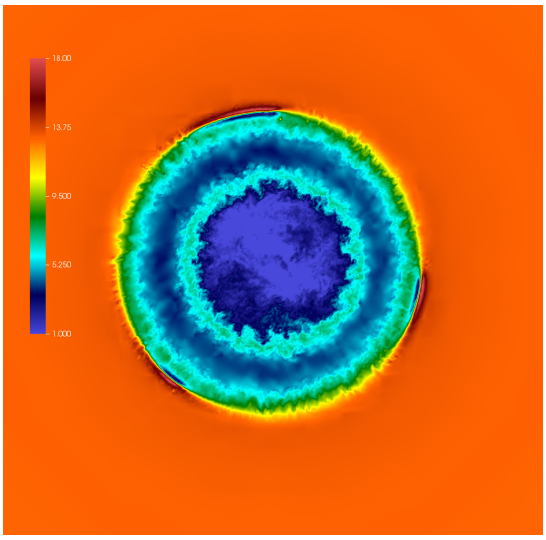

(d) 1D - Design B

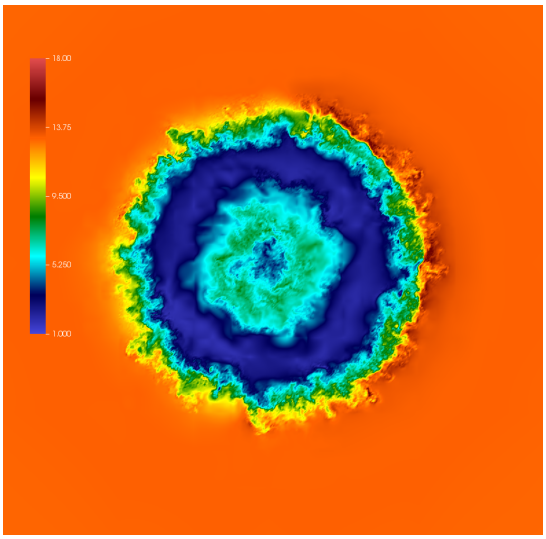

(e) 2D - Design A

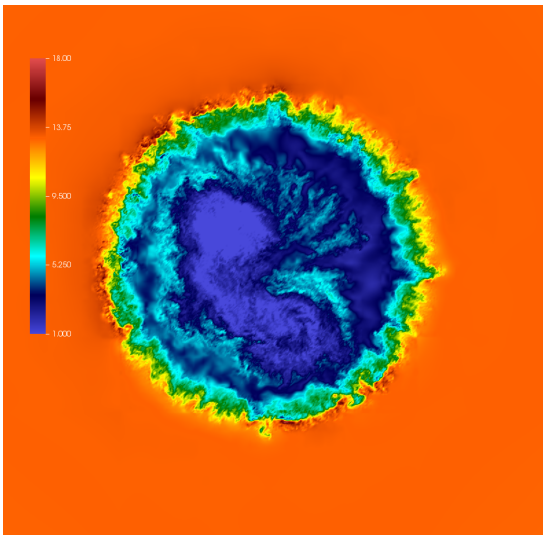

(f) 2D - Design B

Figure 8. Instantaneous axial velocity at down stream wake positions: 0.5, 1.0, and 2.0, rotor diameters(D).

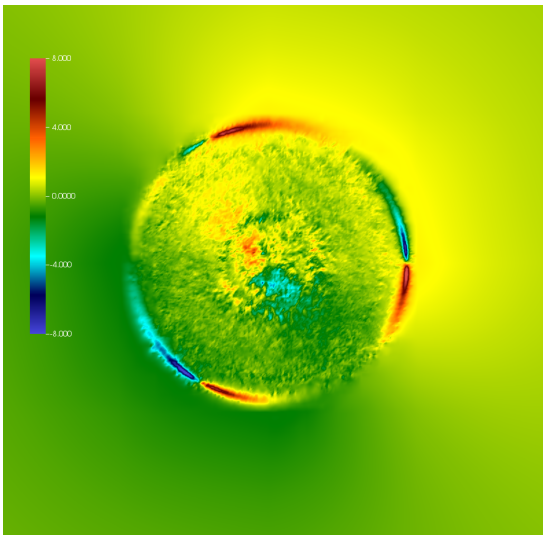

(a) 0.5D - Design A

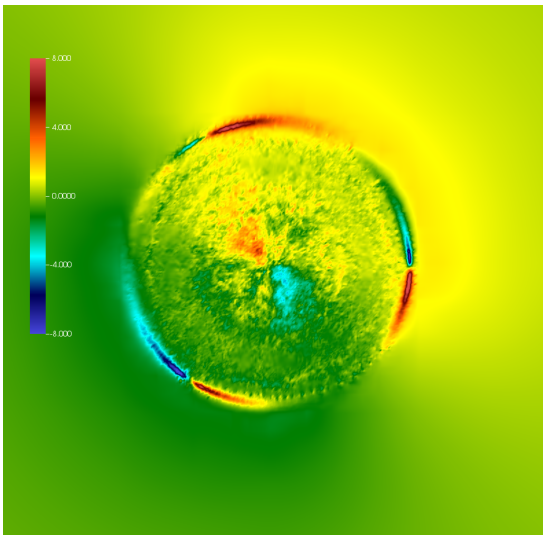

(b) 0.5D - Design B

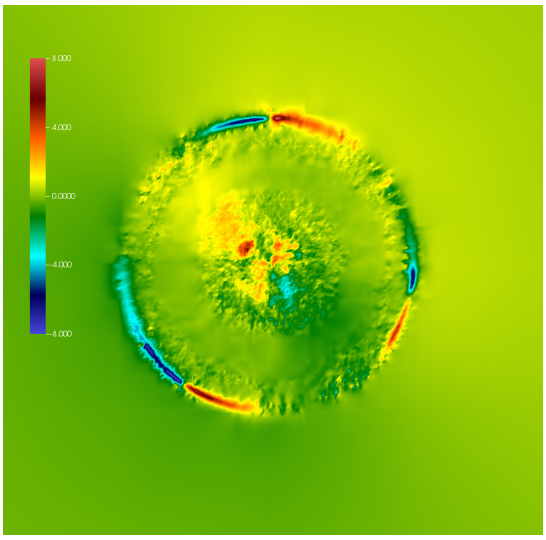

(c) 1D - Design A

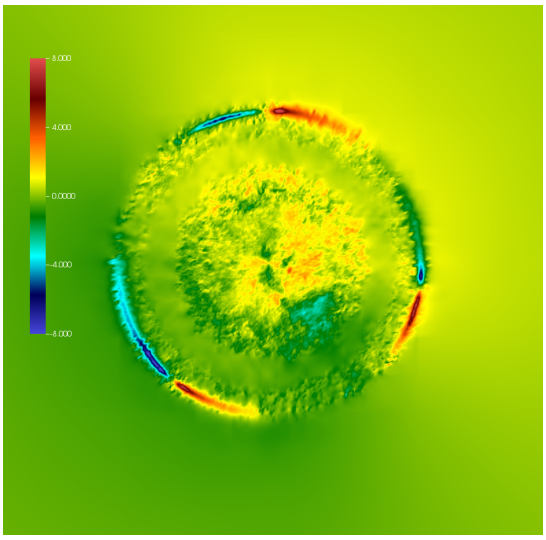

(d) 1D - Design B

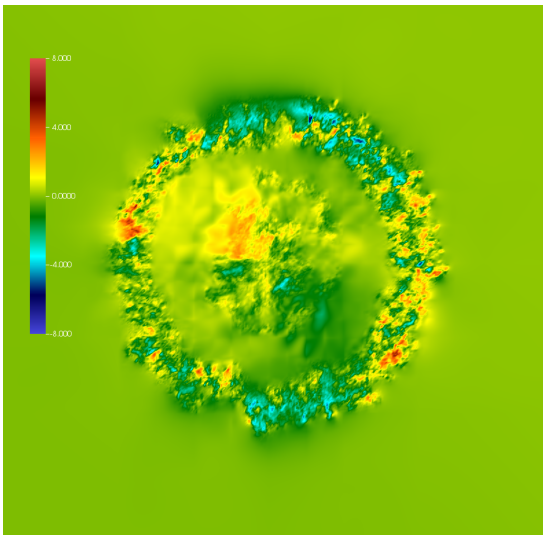

(e) 2D - Design A

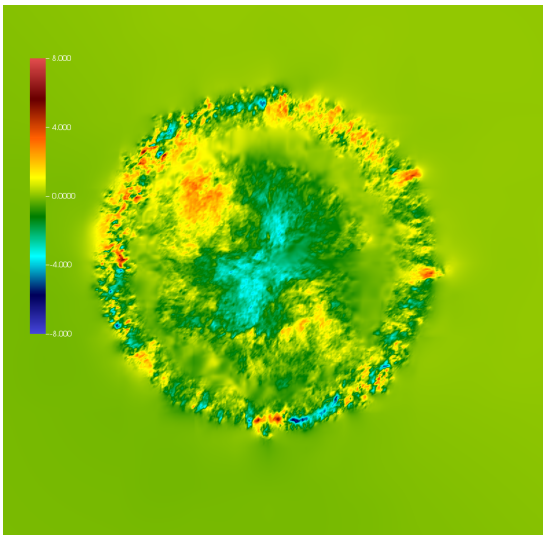

(f) 2D - Design B

Figure 9. Instantaneous radial velocity at down stream wake positions: 0.5, 1.0, and 2.0 rotor diameters(D).

IV.C. Average Velocity Comparison

The slices discussed in the previous section are time averaged over the 2,160 temporal slices corresponding to 12 rotor revolutions. At a given time instance, t_k, there is a given instantaneous velocity U(t), these are used to obtain the time-averaged velocity, with $n = 2,160$:

$$\bar{u} = \frac{\sum_k^n U(t_k)}{n}. \tag{1}$$

The wake velocity fields are discussed for the two designs and quantitative comparison are carried out. The results are presented at two different turbine downstream locations. The axial velocity component is characterized by a significant velocity deficit in both turbines wakes, with some differences in the velocity profile. As shown in Figure 10, at $r/D < 0.3$, the velocity deficit is lower for Design A compared to Design B, however Design B shows lower velocity deficit at $r/D > 0.3$. This result again agrees with the blade loading in Figure 4, where the loading in the inboard position of Design B is higher resulting in the observed higher velocity deficit. Moving downstream to $x/D = 2$, the velocity deficit for Design B drops in the center of the wake and a smoother velocity profile is observed.

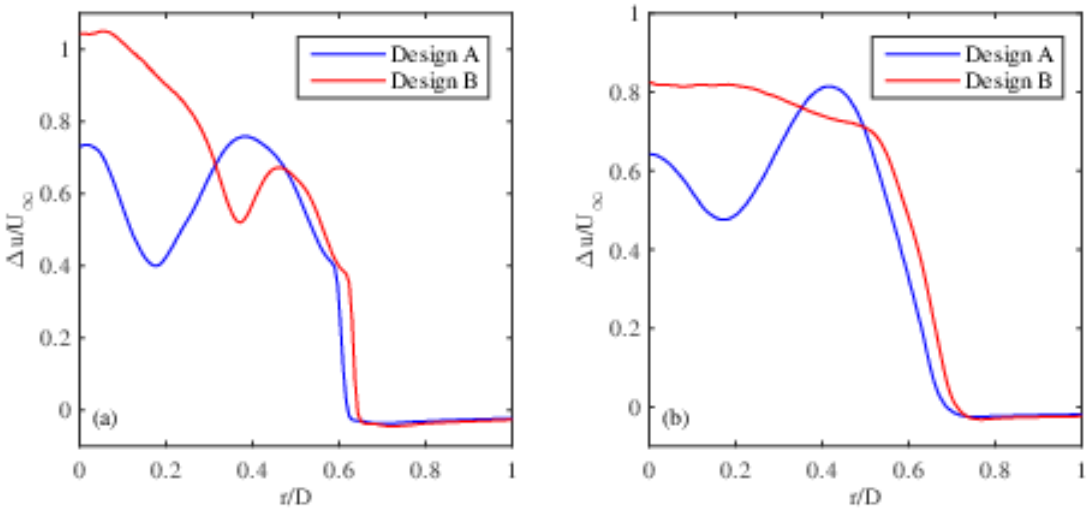

Figure 10. Averaged axial velocity deficit for two designs at different downstream locations: (a) x/D= 1 (b) x/D=2.

Azimuthal velocity is imparted to flow by the tangential force of the blade on the flow. A significant peak of the azimuthal velocity occurs at radial positions $r/D \approx 0.2$ in Figure 11 for Design A, which is caused by the higher tangential force for Design A, as shown in Figure 4, and is connected with the rotational velocity induced by a vortex structure created in the blade root region. The azimuthal velocity reduces very slowly from $x/D = 1$ to $x/D = 2$.

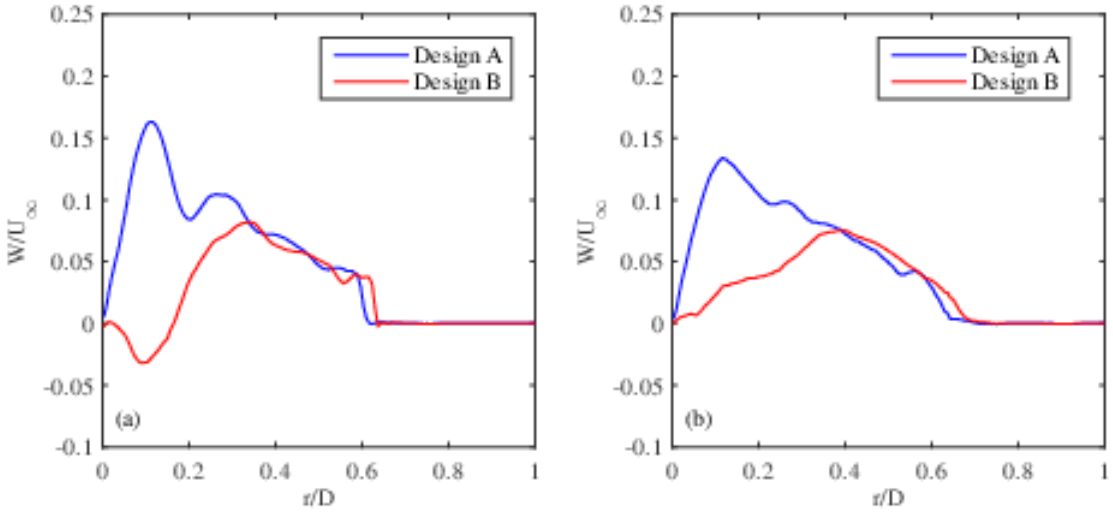

Figure 11. Normalized tangential velocity for two designs at different downstream locations: (a) x/D= 1 (b) x/D=2.

IV.D. Reynolds Stress Analysis

The 2,160 wake slices were used to to temporally average the Reynolds stress. Here, the instantaneous velocity is defined as U(t), at a given time t_k, and the time-averaged velocity as $\bar{u}$, over $n = 2,160$ time instances. The Reynolds stress is calculated with:

$$\overline{u_i u_j} = \frac{\sum_k^n (U_i(t_k) - \bar{u_i})(U_j(t_k) - \bar{u_j})}{n}, u_i = \{u, v, w\} \tag{2}$$

The axial normal stress, $\bar{uu}/U^2$, shown in Figure 12, has an increased intensity in the wake, representing the mechanically produced turbulence due to the presence of the wake velocity deficit. This turbulent energy diffuses and dissipates as the flow travels downstream, while the wake diffuses and increases its width for both designs. Higher axial normal Reynolds stresses can be seen for Design B at $r/D < 0.5$. Again, we see a significant difference in the distributions at $x/D = 2$ that is caused by the load distribution.

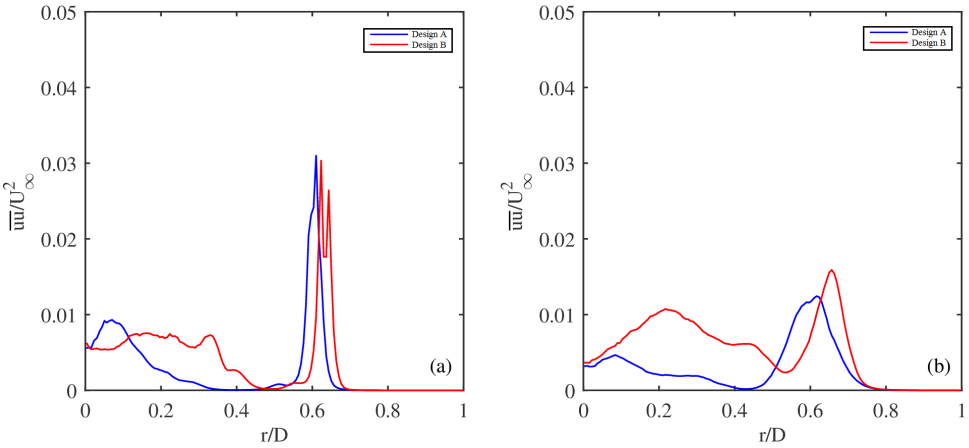

Figure 12. Axial Reynolds stress for two designs at different downstream locations: (a) x/D= 1 (b) x/D=2

However, in Figure 13, the normal stress connected to the azimuthal velocity component at the radial locations related to outboard of the blade increases at downstream locations for the both designs and Design

B shows relatively higher values. This suggests that turbulent energy is being transferred to the azimuthal fluctuations from axial or radial fluctuation.

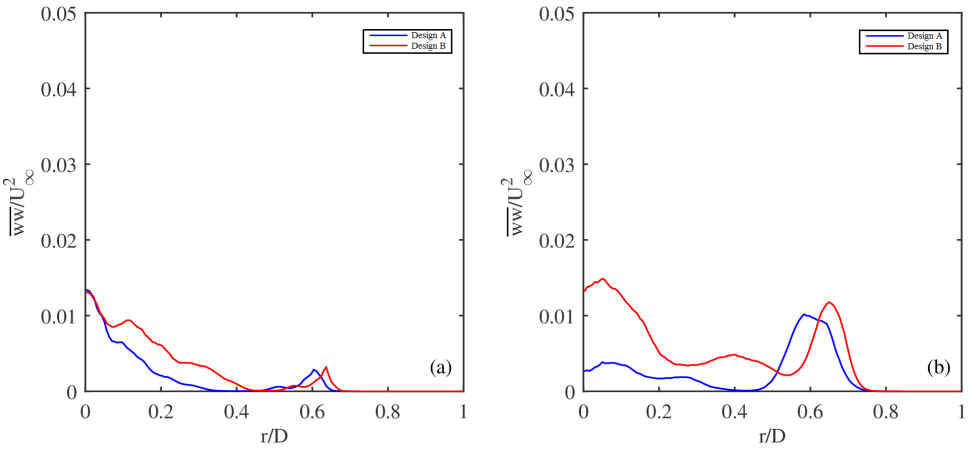

Figure 13. Tangential Reynolds stress for two designs at different downstream locations: (a) x/D= 1 (b) x/D=2

V. Conclusion and Future Work

Blade resolved CFD simulations of two small-scale turbine designs have been completed using a high-fidelity simulation framework. The results show that relatively small differences in blade loading result in significant differences in wake velocity profiles. Both qualitative differences in the instantaneous flow structure, and quantitative differences in the mean and fluctuation velocity statistics highlight these differences in the near wake.

These results indicate the wake is highly sensitive to the blade loading. This implies extreme care should be taken to correctly design experimental turbine blades to capture the important physical phenomena of interest to the industrial scale turbines. The differences in the features in the tip region and also the wake core support this assessment.

Additional work will include studying the wake further downstream for these two turbines. This will reveal how far downstream the different blade load distributions remain significant. Additionally, similarly designed turbines with different blade loadings should be analyzed to provide additional insight.

VI. Acknowledgments

This work is supported in part by ONR Grant N00014-14-1-0045 and by the U.S. Department of Energy, Office of Science, Basic Energy Sciences, under Award DE-SC0012671. Computer time was provided by the NCAR-Wyoming Supercomputer Center (NWSC) and the University of Wyoming Advanced Research Computing Center (ARCC).

References

[1]Kelley, C. L., Maniaci, D. C., and Resor, B. R., "Horizontal-axis wind turbine wake sensitivity to different blade load distributions," *AIAA 33rd Wind Energy Symposium*, 2015, p. 0490.

[2]Yang, X., Boomsma, A., Sotiropoulos, F., Resor, B. R., Maniaci, D. C., and Kelley, C. L., "Effects of spanwise blade load distribution on wind turbine wake evolution," *AIAA 33rd Wind Energy Symposium*, 2015, p. 0492.

[3]Kirby, A. C., Brazell, M. J., Yang, Z., Roy, R., Ahrabi, B. R., Mavriplis, D. J., Sitaraman, J., and Stoellinger, M. K., "Wind Farm Simulations Using an Overset *hp*-Adaptive Approach with Blade-Resolved Turbine Models," AIAA Paper 2017-3958, 23rd AIAA Computational Fluid Dynamics Conference, Denver, CO., June 2017.

[4]Kirby, A. C., Brazell, M. J., Mavriplis, D. J., and Sitaraman, J., "An Overset Adaptive High-Order Approach for Blade-Resolved Wind Energy Applications," AHS Forum 72, West Palm Beach, FL., May 2016.

[5]Brazell, M. J., Kirby, A. C., and Mavriplis, D. J., "A high-order discontinuous-Galerkin octree-based AMR solver for overset simulations," AIAA Paper 2017-3944, 23rd AIAA Computational Fluid Dynamics Conference, Denver, CO., June 2017.

[6]Brazell, M. J., Kirby, A. C., Sitaraman, J., and Mavriplis, D. J., "A multi-solver overset mesh Approach for 3D mixed element variable order discretizations," AIAA Paper 2016-2053, 54th AIAA Aerospace Sciences Meeting, San Diego, CA., June 2016.

[7]Mavriplis, D. J., "Grid resolution study of a drag prediction workshop configuration using the NSU3D unstructured mesh solver," AIAA Paper 2005-729, 23rd AIAA Applied Aerodynamics Conference, Toronto, Ontario Canada, June 2005.

[8]Mavriplis, D. and Long, M., "NSU3D Results for the Fourth AIAA Drag Prediction Workshop," *Journal of Aircraft*, Vol. 51, No. 4, 2014, pp. 1161–1171.

[9]Spalart, P. and Allmaras, S., "A one-equation turbulence model for aerodynamic flows," *30th aerospace sciences meeting and exhibit*, 1992, p. 439.

[10]Wilcox, D. C., "Reassessment of the scale-determining equation for advanced turbulence models," *AIAA journal*, Vol. 26, No. 11, 1988, pp. 1299–1310.

[11]Spalart, P. R., Deck, S., Shur, M., Squires, K., Strelets, M. K., and Travin, A., "A new version of detached-eddy simulation, resistant to ambiguous grid densities," *Theoretical and computational fluid dynamics*, Vol. 20, No. 3, 2006, pp. 181–195.

[12]Shur, M. L., Strelets, M. K., Travin, A. K., and Spalart, P. R., "Turbulence modeling in rotating and curved channels: assessing the Spalart-Shur correction," *AIAA journal*, Vol. 38, No. 5, 2000, pp. 784–792.

[13]Burstedde, C., Ghattas, O., Gurnis, M., Isaac, T., Stadler, G., Warburton, T., and Wilcox, L., "Extreme-scale AMR," *Proceedings of the 2010 ACM/IEEE International Conference for High Performance Computing, Networking, Storage and Analysis*, IEEE Computer Society, 2010, pp. 1–12.

[14]Burstedde, C., Wilcox, L. C., and Ghattas, O., "p4est: Scalable algorithms for parallel adaptive mesh refinement on forests of octrees," *SIAM Journal on Scientific Computing*, Vol. 33, No. 3, 2011, pp. 1103–1133.

[15]Smagorinsky, J., "General circulation experiments with the primitive equations: I. The basic experiment," *Monthly weather review*, Vol. 91, No. 3, 1963, pp. 99–164.

[16]Roget, B. and Sitaraman, J., "Robust and efficient overset grid assembly for partitioned unstructured meshes," *Journal of Computational Physics*, Vol. 260, 2014, pp. 1–24.

[17]Brazell, M. J., Sitaraman, J., and Mavriplis, D. J., "An overset mesh approach for 3D mixed element high-order discretizations," *Journal of Computational Physics*, Vol. 322, 2016, pp. 33–51.

[18]Crabill, J. A., Sitaraman, J., and Jameson, A., "A High-Order Overset Method on Moving and Deforming Grids," *AIAA Modeling and Simulation Technologies Conference*, 2016, p. 3225.

[19]Hassanzadeh, A., Naughton, J. W., Kelley, C. L., and Maniaci, D. C., "Wind turbine blade design for subscale testing," *Journal of Physics: Conference Series*, Vol. 753, IOP Publishing, 2016, p. 022048.